

Evidence for a Massive Protocluster in S255N

C.J. Cyganowski¹, C.L. Brogan², T.R. Hunter²

ccyganow@astro.wisc.edu

cbrogan@nrao.edu

thunter@nrao.edu

ABSTRACT

S255N is a luminous far-infrared source that contains many indications of active star formation but lacks a prominent near-infrared stellar cluster. We present mid-infrared through radio observations aimed at exploring the evolutionary state of this region. Our observations include 1.3 mm continuum and spectral line data from the Submillimeter Array, Very Large Array 3.6 cm continuum and 1.3 cm water maser data, and multicolor IRAC images from the *Spitzer Space Telescope*. The cometary morphology of the previously-known UCH II region G192.584-0.041 is clearly revealed in our sensitive, multi-configuration 3.6 cm images. The 1.3 mm continuum emission has been resolved into three compact cores, all of which are dominated by dust emission and have radii < 7000 AU. The mass estimates for these cores range from 6 to 35 M_{\odot} . The centroid of the brightest dust core (SMA1) is offset by 1.1'' (2800 AU) from the peak of the cometary UCH II region and exhibits the strongest HC_3N , CN , and DCN line emission in the region. SMA1 also exhibits compact CH_3OH , SiO , and H_2CO emission and likely contains a young hot core. We find spatial and kinematic evidence that SMA1 may contain further multiplicity, with one of the components coincident with a newly-detected H_2O maser. There are no mid-infrared point source counterparts to any of the dust cores, further suggesting an early evolutionary phase for these objects. The dominant mid-infrared emission is a diffuse, broadband component that traces the surface of the cometary UCH II region but is obscured by foreground material on its southern edge. An additional $4.5 \mu\text{m}$ linear feature emanating to the northeast of SMA1 is aligned with a cluster of methanol masers and likely traces a outflow from a protostar within

¹University of Wisconsin, Madison, WI 53706

²NRAO, 520 Edgemont Rd, Charlottesville, VA 22903

SMA1. Our observations provide direct evidence that S255N is forming a cluster of intermediate to high-mass stars.

Subject headings: stars: formation — infrared: stars — ISM: individual (S255N) — ISM: individual (G192.60-MM1) — ISM: individual (G192.584-0.041) — techniques: interferometric — submillimeter

1. Introduction

The formation and early evolution of stellar clusters occurs in deeply embedded regions of giant molecular clouds (Lada & Lada 2003). While much has been learned from recent surveys in the infrared (Gutermuth et al. 2005; Muench et al. 2002), the earliest stages of cluster formation will (at least in many cases) be hidden from all but the longest IR/millimeter wavelengths. Due to the small size scales of young clusters—multiplicity of protostars has been observed on scales of a few thousand AU (e.g. Megeath, Wilson, & Corbin 2005)—high angular resolution is necessary to resolve individual objects, particularly in massive star forming regions which lie at relatively large distances (> 1 kpc). These considerations point to millimeter-wavelength interferometric observations of thermal dust continuum emission as an effective means of searching for clusters of young protostars, as the mm emission remains optically thin up to high column densities ($N_{\text{H}} \sim 10^{25} \text{ cm}^{-2}$).

Located $\sim 1'$ north of the luminous infrared cluster S255IR, S255N is a promising target in the search for young protoclusters. As illustrated in Figure 1, S255N is located in a complicated region of past and ongoing massive star formation. S255N and S255IR (saturated in this mid-IR *Spitzer* IRAC image) lie between two large H II regions, S255 and S257. Large-scale ^{12}CO and HCN observations show that S255IR and S255N occupy opposite ends of a molecular ridge between the H II regions (Heyer et al. 1989). The total luminosity of S255N ($\sim 1 \times 10^5 L_{\odot}$) is about twice that of S255IR (Minier et al. 2005), and single-dish continuum and spectral line observations at submillimeter and millimeter wavelengths have established the presence of large column densities of dust and gas toward both regions (e.g. Richardson et al. 1985; Mezger et al. 1988; Zinchenko, Henning, & Schreyer 1997; Minier et al. 2005). Observations at infrared and radio wavelengths, however, suggest that S255N is the younger of the two regions. For example, S255IR is bright (> 70 Jy) in all infrared bands of the *Midcourse Space Experiment (MSX)* and contains a well-developed near-IR cluster of early-B type stars (S255-2 Howard, Pipher & Forrest 1997; Itoh et al. 2001), a cluster of compact H II regions (Snell & Bally 1986), and a wealth of complex H_2 emission features (Miralles et al. 1997). In contrast, S255N (also called S255 FIR1 and G192.60-MM1) is undetected in *MSX* images at wavelengths shorter than

21 μm (Crowther & Conti 2003), and contains only a single cometary UC H II region, G192.584-0.041 (e.g. Kurtz, Churchwell, & Wood 1994).

Additional evidence for protostellar activity in S255N exists in the form of outflow tracers. For example, two small knots of H_2 emission bracket the UC H II region and may be tracing an outflow (Miralles et al. 1997). In beamsizes of $\sim 50''$, redshifted CO emission (Heyer et al. 1989) and highly-blueshifted OH absorption (Ruiz et al. 1992) are also seen toward the UC H II region. Finally, 44 GHz (7_0-6_1) A^+ Class I methanol masers form a linear feature extending northeast of the UC H II region (Kurtz, Hofner, & Álvarez 2004); masers of this type have been observed in association with molecular outflows in other objects (Plambeck & Menten 1990; Kurtz, Hofner, & Álvarez 2004).

At this stage, further understanding of the state of star formation in S255N requires resolving the mm dust continuum emission in order to search for additional compact sources that may be present in the vicinity of the UC H II region. The high angular resolution now available with the Submillimeter Array (SMA)¹ makes this goal possible, while the wide bandwidth allows simultaneous observation of many spectral lines, which are sensitive to a range of gas conditions across the region. We describe our observations in section 2, present our results in section 3, and discuss our interpretations in section 4.

A range of distances to S255 and S255N have been used in the literature. At the extremes, Georgelin, Georgelin, & Roux (1973) find an optical distance of 3.2 kpc to each of the adjacent H II regions S254 and S257 (located west of S255N), while Hunter & Massey (1990) find a distance of 1.1 kpc to the optical H II region S255 (located east of S255N, see Figure 1) based on spectroscopy of its exciting star. Using a LSR velocity of $+9 \text{ km s}^{-1}$ (typical of the centroid velocities of our observed lines), and a Galactic center distance of 8.5 kpc, we find a kinematic distance to S255N of 2.2 kpc using the rotation curve of Brand & Blitz (1993). In this paper we adopt a distance of 2.6 kpc for S255N (also see Moffat et al. 1979; Minier et al. 2005).

¹The Submillimeter Array is a joint project between the Smithsonian Astrophysical Observatory and the Academia Sinica Institute of Astronomy and Astrophysics and is funded by the Smithsonian Institution and the Academia Sinica.

2. Observations

2.1. Submillimeter Array (SMA)

Our SMA observations toward S255N were obtained on December 06, 2003 in the compact configuration. Six antennas were operational and the projected baseline lengths ranged from 12 to 62 k λ , resulting in a synthesized beam of $4''.7 \times 2''.4$ (P.A. = -45.65°). In this configuration, the interferometer is not sensitive to smooth structures larger than $17''$. The phase center was $06^{\text{h}}12^{\text{m}}53^{\text{s}}.56$, $18^\circ00'25''.0$ (J2000), and the double-sideband SIS receivers were tuned to an LO frequency of 222.78 GHz. With a bandwidth of ~ 2 GHz, the correlator covered 216.796–218.764 GHz in lower sideband (LSB) and 226.796–228.764 GHz in upper sideband (USB). The data were resampled to provide uniform spectral resolution of 1.12 km s^{-1} . The zenith opacity as measured by the 225 GHz tipping radiometer at the Caltech Submillimeter Observatory (CSO) was 0.18 at the beginning of the observations and fell as low as 0.16. Data recorded late in the observing session, when the opacity had climbed to 0.3, were not used. The typical system temperature at source transit was 200 K. The primary beamsize of the 6-meter SMA antennas at this frequency is $56''$.

Initial calibration of the data was performed in Miriad. The gain calibrators were J0739+016 and J0423-013. J0423-013 was also used for passband calibration. Subsequent processing was carried out in AIPS. The continuum emission was measured using line-free channels and removed in the $u-v$ plane. The resulting continuum-only data were then self-calibrated; these complex gain solutions were also applied to the continuum-subtracted line data. The absolute position uncertainty is estimated to be $0.''3$ and the amplitude calibration is accurate to 20%. For maximum sensitivity, both the continuum and line data were imaged with natural weighting. The rms sensitivity of the continuum image is 4 mJy beam^{-1} (8 mK) and the rms sensitivity of the line data is 89 mJy beam^{-1} (170 mK).

2.2. Very Large Array (VLA)

Archival 3.6 cm data from the NRAO² Very Large Array (VLA) were calibrated and imaged in AIPS. The observation date was 2003 June 15 and the total time on source was ~ 70 minutes (project code AH819). The VLA was in A-configuration, in which the interferometer is not sensitive to smooth structures larger than $\sim 7''$. The bandwidth was 50 MHz in two IFs. The flux calibrator was 3C147, and the gain calibrator was J0613+131.

²The National Radio Astronomy Observatory is a facility of the National Science Foundation operated under agreement by the Associated Universities, Inc.

The synthesized beam of the 3.6 cm continuum image is $0''.27 \times 0''.23$ (P.A.= 77.51°) and the rms sensitivity is $18 \mu\text{Jy beam}^{-1}$. Archival 3.6 cm data from the B configuration (in which the interferometer is not sensitive to smooth structures larger than $\sim 20''$), observed on 1990 August 27 (project code AM301), and from the the CnB configuration, observed on 2005 June 21 (project code TSTCJC), were also reduced and combined with the A-configuration data. The resulting image, made with a UV taper at $500 \text{ k}\lambda$, has a synthesized beam of $1''.03 \times 0''.84$ (P.A.= -81.42°) and a rms sensitivity of $34 \mu\text{Jy beam}^{-1}$.

Archival 1.3 cm data from the VLA A-configuration (project code AC299) were analyzed for water maser emission at 22.235 GHz. The observation date was 1991 August 1, total on-source integration time was ~ 10 minutes. The phase center of this observation was toward the IR cluster $\sim 1'$ to the south of S255N, hence a correction for the primary beam attenuation has been applied to the data. The bandpass calibrator was 3C84 and the flux calibration was derived assuming a flux density of 2.16 Jy for J0528+134. The synthesized beam is $0''.18 \times 0''.16$ (P.A.= -56.55°), the spectral line channel spacing is 0.33 km s^{-1} , and the rms noise is $0.13 \text{ Jy beam}^{-1}$.

2.3. Spitzer Space Telescope

Mid-infrared images of S255 were obtained with the IRAC camera (Fazio et al. 2004) on the *Spitzer Space Telescope* as part of Guaranteed Time Observations program 201 (P.I. G. Fazio) on 12 March 2004. Integrations of 0.4 s and 10.4 s were taken in the high dynamic range mode; S255N is not saturated in the longer exposures, and only the 10.4 s exposures are discussed in this paper. Four 10.4 s exposures covered S255N, for a total integration time on S255N of 41.6 s. Mosaiced post-BCD 3.6, 4.5, 5.8, and $8.0 \mu\text{m}$ images, calibrated and processed using pipeline version S13.2.0, were downloaded from the *Spitzer* data archive.

2.4. Caltech Submillimeter Observatory

Our submillimeter continuum observations were obtained at the CSO using the Submillimeter High Angular Resolution Camera (SHARC), a ^3He -cooled monolithic silicon bolometer array of 24 pixels in a linear arrangement (Hunter, Benford & Serabyn 1996; Wang et al. 1996). For a typical dust source with a submillimeter spectral index of ~ 4 , the effective frequency of the broadband $350 \mu\text{m}$ filter is 852 GHz and the bandwidth is 103 GHz. An on-the-fly (OTF) map of S255 was obtained on 21 December 1995 by scanning the array through the source in azimuth while the secondary mirror was chopping at a rate of 4.1

Hz and a throw of $88''$. Successive scans were made after stepping the array in elevation by increments of $5''$. Airmass corrections were applied to each scan using the opacity derived from frequent scans of Saturn during the night. The map data were restored with a NOD2 dual beam restoration algorithm (Emerson, Klein & Haslam 1979) and transformed into equatorial coordinates. The resulting image was smoothed with a Gaussian to produce an effective half-power beamsize of $15''$.

3. Results

3.1. Continuum emission

Our 1.3 mm SMA continuum data resolve three distinct sources within the previously-observed submm/mm clump of S255N (aka S255 FIR1 and G192.60-MM1: Jaffe et al. 1984; Mezger et al. 1988; Minier et al. 2005). Figure 2 shows the SMA 1.3 mm continuum image with CSO 350 μm contours superposed. As illustrated in Figure 2, the strongest SMA 1.3 mm emission peak coincides with the CSO 350 μm peak (resolution $15''$). The CSO 350 μm integrated flux density is 575 ± 20 Jy, consistent to within 10% of the value predicted by the dust spectral energy distribution (SED) models of Minier et al. (2005). The three mm sources resolved with the SMA are designated SMA1, SMA2, and SMA3 in order of descending peak intensity. The observed properties of each source (peak intensity, brightness temperature, integrated flux density, and source size) are listed in Table 1, and the sources are labeled in Figure 2. The integrated flux densities and source sizes listed in Table 1 were determined by fitting a single Gaussian component to each SMA source. SMA1 was not well fit by a single Gaussian, indicating that the observed continuum emission may arise from multiple sources unresolved by the SMA beam; this issue is discussed further in §4.2. The total flux density of the three compact mm sources is 0.79 ± 0.16 Jy; stated errors include the 20% uncertainty in flux calibration. This total corresponds to $15 \pm 3\%$ of the single-dish flux density measured by Minier et al. (2005) with the SEST 15m telescope at 1.2mm (resolution $24''$).

Figure 3 compares the morphology of the 1.3 mm dust continuum emission with the 3.6 cm free-free continuum emission from the cometary UC HII region, G192.584-0.041. Figure 3a shows the lower-resolution ($1''.03 \times 0''.84$) 3.6 cm VLA image superposed on the SMA 1.3 mm continuum, while Figure 3b shows the high-resolution VLA 3.6 cm image ($0''.27 \times 0''.23$), with the positions of the newly-reported water maser (see §3.2) and the Class I methanol masers detected by Kurtz, Hofner, & Álvarez (2004) indicated.

The $\sim 1''$ resolution 3.6 cm VLA image presented in Figure 3a provides the most detailed

view to date of the diffuse cometary “tail” of the UC H II region. The integrated flux density of G192.584-0.041 measured from this image is 26.0 ± 0.1 mJy. Based on our measurement and published 2 cm integrated flux densities for G192.584-0.041 (Kurtz, Churchwell, & Wood 1994; Rengarajan & Ho 1996), the spectral index from 3.6 cm to 2 cm is ~ -0.1 , consistent with optically thin free-free emission. The flux density is consistent with a single exciting star of spectral type B0.5 (as determined by Kurtz, Churchwell, & Wood 1994; Snell & Bally 1986). Extrapolating to 1.3 mm, we estimate the free-free contribution of G192.584-0.041 to the 1.3 mm flux density of SMA1 to be $\lesssim 20$ mJy ($\leq 3.5\%$).

The 3.6 cm VLA image presented in Figure 3b is the highest-resolution cm-wavelength image of G192.584-0.041 to date. With a resolution of $0''.27 \times 0''.23$, the continuum emission from G192.584-0.041 is resolved into three components (east to west): an arc, a point source, and an extended feature (the extended “tail” is resolved out in the higher resolution data). All three of these components overlap with the eastern side of SMA1, but none is coincident with the mm emission peak, in agreement with the estimate that the free-free contribution at 1.3 mm is quite small. The arc, which is oriented with its convex side towards the mm peak, contains the brightest 3.6 cm emission. The 3.6 cm peak is located in the southern part of the arc, east of the point source, and is offset by $1''.1$ (~ 2800 AU) from the location of the SMA1 mm continuum peak determined by fitting a single Gaussian component. The 3.6 cm point source, which is located west of the arc and faces its concave side, is offset by $1''.6$ ($\sim 4,200$ AU) from the SMA1 mm continuum peak. The peak brightness temperature of the 3.6 cm point source is only 122 K at the current resolution. Absent a second radio frequency image with comparable resolution, it is not currently possible to ascertain the spectral indices of the individual components. The 3.6 cm images presented in Figure 3(a-b) place strong limits on the presence of any additional H II regions in S255N. Other than G192.584-0.041, no cm-wavelength emission is detected down to a 5σ limit of $90 \mu\text{Jy beam}^{-1}$ (high-resolution image).

3.2. Water maser emission

Water maser emission was detected at the position $06^{\text{h}}12^{\text{m}}53^{\text{s}}.71$, $18^{\circ}00'27''.6$ (J2000), offset $0''.9$ ($\sim 2,300$ AU at 2.6 kpc) to the northeast of the 1.3 mm continuum emission peak of SMA1, as determined by fitting a single Gaussian component. This is the first report of water maser emission from S255N. The peak intensity is 2.8 Jy beam^{-1} (corrected for primary beam attenuation) at $v_{\text{LSR}} = +8.5 \text{ km s}^{-1}$. The line is barely resolved by the 0.33 km s^{-1} spectral resolution.

The positions of the Class I 44 GHz (7_0-6_1) A⁺ methanol masers detected by Kurtz, Hofner, & Álvarez

(2004) are marked with crosses in Fig. 3b, which shows the 1.3 mm and 3.6 cm continuum emission and the newly-reported water maser. Kurtz, Hofner, & Álvarez (2004) estimate an astrometric uncertainty of $0''.5$ for the CH_3OH maser spots, while the absolute astrometry of the H_2O maser is better than $0''.1$. The position of one of the CH_3OH maser spots is consistent with SMA1, within the astrometric uncertainty. The newly detected water maser is $< 1''$ from two CH_3OH masers, and falls into the linear pattern of 44 GHz (7_0-6_1) A^+ CH_3OH maser spots that extends northeast from SMA1.

3.3. Line emission

Molecular line emission from H_2CO , CH_3OH , SiO , CN , DCN , and HC_3N is detected in S255N; the specific transitions, frequencies, and upper state energies are listed in Table 2. The lines detected in S255N are the same as those detected in the spectral regions covered by our sidebands by Sutton et al. (1985) in their line survey of the Orion A molecular cloud, which is similar to our data in spectral resolution (1.3 km/s), rms sensitivity (0.2 K), and linear size scale ($30'' = \sim 13,500$ AU at 450 pc). Integrated intensity images for CH_3OH , SiO , and H_2CO are presented in Figure 4(a-d) and for DCN , HC_3N , and CN in Figure 5(a-c). The distributions of molecular emission observed in S255N fall into two main categories: CH_3OH , H_2CO and SiO exhibit emission from multiple locations, while DCN and HC_3N are detected only in the vicinity of SMA1. CN exhibits compact emission towards SMA1, and is also weakly detected toward SMA3. The CN lines have the lowest E_{upper} of the observed transitions, and the CN images show artifacts from large-scale emission resolved out by the interferometer, suggesting that much of the CN emission originates in an extended, cool envelope around the compact continuum sources.

As shown in Figure 4(a-d), the spatial distributions of the integrated emission from H_2CO , CH_3OH , and SiO are similar to one another. The kinematics of these molecules are complex, as illustrated in Figures 6 and 7, with multiple spatially and kinematically distinct components apparent. A finder chart for the positions of the profiles displayed in Fig. 7 (named after their relative positions with respect to SMA1) is shown in Figure 5(d). The positions are listed in Table 3. Line centroid velocities, Δv_{FWHM} , and integrated line intensities obtained from Gaussian fits to the line profiles at these positions are listed in Table 4. Unless otherwise noted, the fit parameters in Table 4 are for the strongest component in the spectrum. Fits to SiO line profiles are not included because the SiO line shapes are so complex.

The strongest molecular emission in S255N lies toward the “SW” position $\sim 6''$ to the southwest of SMA1 at a peak velocity between $\sim 6 - 8$ km s $^{-1}$ (Figs. 4, 6, 7c, Table 4).

This molecular emission is not coincident with any mm continuum emission and overlaps the southern edge of the extended “tail” of the UC H II region (Fig. 4). The line emission toward the “SW” position is broader than at any other location in S255N, with $\Delta v_{FWHM} \sim 7$ and 9 km s^{-1} for CH_3OH and H_2CO , respectively, and shows pronounced blue wings. The velocity of the H_2CO peak is slightly more blueshifted than CH_3OH , while SiO is significantly blueshifted relative to both H_2CO and CH_3OH (Fig. 7c, Table 4).

The second-brightest region of H_2CO , CH_3OH , and SiO emission in S255N is located in the vicinity of SMA1, east of the cometary head of the UCH II region (Fig. 4). DCN, CN, and HC_3N have their strongest emission in this area (Fig. 5). Spectral line profiles for DCN, CN, and HC_3N are shown in Figure 8 and channel maps for DCN are shown in Figure 9. Two positionally and kinematically distinct components are evident in H_2CO , DCN, CN, HC_3N , and weakly, CH_3OH , in the vicinity of SMA1. One component (denoted SMA1-NE) lies $1''.21$ to the northeast of the SMA1 mm peak at a velocity of $\sim 7 \text{ km s}^{-1}$, and the other (denoted SMA1-SW) lies $1''.17$ southwest of the SMA1 mm peak at $\sim 11.5 \text{ km s}^{-1}$ (Figs. 6, 7a,b, and 8a,b). SMA1-SW is $1''.08$ east of the 3.6 cm point source.

Interestingly, SMA1-NE and SMA1-SW also show differences in their chemical properties. For example, H_2CO shows nearly equal strength towards both positions, as does HC_3N , while CH_3OH is much stronger toward SMA1-SW (Fig. 6, 8). In contrast, DCN and CN are both significantly stronger toward SMA1-NE (Fig. 8). Some differences in the peak velocities at the two positions are also apparent amongst species. Relative to the other molecules, SiO is significantly blueshifted ($v_{LSR} < 5 \text{ km s}^{-1}$) towards both SMA1-SW and SMA1-NE (Fig. 7, Table 4). DCN is slightly redshifted relative to CN and HC_3N toward both positions (Fig. 8, Table 4). The CN and HC_3N lines are also more than twice as broad as those of H_2CO or CH_3OH toward SMA1-SW (Table 4).

The H_2CO , CH_3OH , and SiO integrated intensity peak located $\sim 5''$ north of the mm continuum source SMA2 (Fig. 4, “NW” position in Fig. 5d), is comprised of relatively weak, broad emission (Fig. 7f). The H_2CO and CH_3OH lines are narrower than at the SW position, but broader than at any of the other positions (Table 4). As at the other positions, the peak of the SiO line profile is blueshifted relative to H_2CO and CH_3OH (Fig. 7f).

The line emission north and northeast of the SMA1 region (“N” and “NE” positions, finding chart Fig. 5d) consists of narrow velocity features in CH_3OH and H_2CO , and, at the NE position, SiO (Figs. 6 & 7d-e). In contrast to the other positions, at the NE position CH_3OH , H_2CO , and SiO have the same velocity, $v_{LSR} \sim 8 \text{ km s}^{-1}$ (Fig. 7d, Table 4). The velocity of the H_2CO and CH_3OH emission at the N position is similar to the $v_{LSR} \sim 11.5 \text{ km s}^{-1}$ component toward SMA1-SW (Table 4). The H_2CO and CH_3OH lines are narrow, and the CH_3OH peak is slightly blueshifted relative to H_2CO . Broad and

weak blueshifted SiO emission is also detected at this position (Table 4, Fig. 7e).

3.4. Spitzer Space Telescope IRAC Observations

Figure 10 shows a three-color IRAC image (red 8.0 μm , green 4.5 μm , blue 3.6 μm) of S255N, overlaid with contours of the 1.3 mm continuum emission (yellow) and the 3.6 cm continuum emission (white). The positions of the Class I CH₃OH masers reported by Kurtz, Hofner, & Álvarez (2004) and the newly-reported water maser are marked with crosses. Most of the observed mid-IR emission is offset to the northwest of the UC H II region, and this diffuse emission appears in all IRAC bands. An exception is the linear, green 4.5 μm emission feature that extends NE from the SMA1 mm continuum peak. No mid-IR emission is associated with either SMA2 or SMA3, indeed these two positions are notably absent of IR emission.

4. Discussion

4.1. Mass estimates from the dust emission

With an estimate of the dust temperature, we can estimate the masses of the compact dust sources SMA1, SMA2, and SMA3 using a simple isothermal model of optically thin dust emission (Beltrán et al. 2006):

$$M_{\text{gas},\text{thin}} = \frac{R F_{\nu} D^2}{B(\nu, T_d) \kappa_{\nu}} \quad (1)$$

where R is the gas-to-dust mass ratio (assumed to be 100), F_{ν} is the observed flux density, D is the distance to the source, $B(\nu, T_d)$ is the Planck function, and κ_{ν} is the dust mass opacity coefficient. At 1.3 mm, the value of κ for gas densities of 10^6 - 10^8 cm^{-3} does not differ much for grains with thick or thin ice mantles; we adopt a value of $\kappa_{1.3\text{mm}} = 1 \text{ cm}^2 \text{ g}^{-1}$ for all of the compact mm sources (Ossenkopf & Henning 1994). The assumption of low optical depth is justified by the low observed millimeter brightness temperatures (Table 1), however, for highest accuracy we have made the small correction to our derived masses for non-zero optical depth using the formula: $M_{\text{gas}} = M_{\text{gas},\text{thin}} \tau / (1 - e^{-\tau})$.

Previous determinations of the dust temperature and mass in S255N have relied on fitting multiple components to the (unresolved) mid-IR to mm SED. Minier et al. (2005) fit a hot, compact core ($T = 106 \text{ K}$, diameter = 400 AU) and an extended warm envelope ($T = 44 \text{ K}$, diameter = 58,000 AU) to a SED comprised of *MSX*, *IRAS*, *SCUBA*, and *SEST* data,

assuming a distance of 2.6 kpc. The derived luminosity and gas mass are $1.1 \times 10^5 L_\odot$ and $220 M_\odot$, respectively. While many of the datapoints in the SED constructed by Minier et al. (2005) blend emission from all three SMA sources, the very compact hot core implied by their fits would be unresolved by our SMA beam ($\sim 12,200 \times 6,200$ AU at 2.6 kpc). Thus, the hot core temperature of 106 K derived from the SED modeling provides an upper limit for the dust temperature of the compact SMA sources. The fitted warm envelope temperature of 44 K is likewise a good lower limit to the temperature of SMA1 since it dominates the 1.3 mm flux, contributing 73% of the total SMA flux density.

Several single dish estimates of the gas temperature are also available. For example, Effelsberg 100-m observations of NH_3 (1,1) and (2,2) (resolution $40''$) suggest that the kinetic temperature of the gas is only $T_{kin} = 23 \pm 1$ K (Zinchenko, Henning, & Schreyer 1997). Measurements of $\text{CH}_3\text{C}_2\text{H}$ (6-5) $K=0-3$ toward S255N with the Onsala 20-m (resolution $38''$) by Malafeev et al. (2005) yield $T_{rot} = 35 \pm 1$ K, in better agreement with the extended warm component derived for the dust. These authors find significantly higher temperatures using $\text{CH}_3\text{C}_2\text{H}$ (6-5) than NH_3 towards all five sources observed (including S255) and suggest that methyl acetylene may preferentially trace warmer/denser gas. In any case, since beam dilution may play a significant role in these single dish estimates, they can only provide a lower limit to the gas temperatures on SMA sizescales.

From our SMA line data it is clear that SMA1 is the warmest of the compact mm sources: the two detected transitions with the highest E_{upper} (both HC_3N , $E_{upper}=131$ K and 142 K) are detected only towards SMA1, suggesting this may be a hot core (e.g. Hatchell, Millar, & Rodgers 1998). DCN is also seen at this warm position. Though DCN is formed in cold clouds, in this case it can serve as a young hot core tracer since its presence in this warm region suggests it has recently been liberated from the icy mantles of dust grains (e.g. Mangum et al. 1991). The HC_3N emission is consistent with an upper temperature limit of ~ 100 K; a more quantitative determination is not possible with only two observed transitions. In contrast, the ratio of the $\text{H}_2\text{CO}(3_{0,3}-2_{0,2})$ and $\text{H}_2\text{CO}(3_{2,2}-2_{2,1})$ lines is a reliable density-independent temperature diagnostic for $T_K \lesssim 50$ K, and $N(\text{para-}\text{H}_2\text{CO})/\Delta v \lesssim 10^{13.5} \text{ cm}^{-2} (\text{km s}^{-1})^{-1}$ (Mangum & Wootten 1993). In this regime, the $3_{0,3}-2_{0,2}/3_{2,2}-2_{2,1}$ ratio ranges from 15 to 5 for $T_k=20$ to 50 K. In contrast, the observed line ratios in S255N are less than 2.5 throughout the imaged region and are smallest (~ 1.5) toward SMA1, suggesting that the column density (i.e. opacity) and/or temperature is too high for these lines to be diagnostic. For the position of SMA1-NE, assuming a temperature of 75 K, $N_{\text{H}_2\text{CO}} \sim 3.7 \times 10^{13} \text{ cm}^{-2}$ from the $\text{H}_2\text{CO}(3_{0,3}-2_{0,2})$ line and $N_{\text{H}_2\text{CO}} \sim 1.0 \times 10^{14} \text{ cm}^{-2}$ from the $\text{H}_2\text{CO}(3_{2,2}-2_{2,1})$. This comparison suggests that the $3_{0,3}-2_{0,2}$ line is moderately optically thick compared to the $3_{2,2}-2_{2,1}$ line, and that the low line ratios are a combination of both the column density and temperature being higher than the diagnostic range of these two

transitions. Combining this analysis with the SED models and the single dish line results described above, the allowed temperature range for SMA1 is 40 - 100 K. The resulting ranges of gas mass, column density, and number density computed for SMA1 are shown in Table 5. The high derived gas density ($n_{H_2} \sim 3\text{--}16 \times 10^6 \text{ cm}^{-3}$), also implied by the presence of the water maser, indicates that the gas and dust temperatures are likely to be well-coupled (e.g. Kaufman, Hollenbach, & Tielens 1998; Ceccarelli, Hollenbach & Tielens 1996).

Unlike SMA1, SMA2 and SMA3 are not accompanied by significant line emission. H_2CO , CH_3OH , and SiO emission are present to the north of SMA2, and CN emission is detected toward SMA3 (§3.3), but the physical relationship (if any) between this line emission and the dust continuum sources is unclear. Also unlike SMA1, SMA2 and SMA3 are not associated with mid-IR emission in any IRAC band (§3.4). Instead, SMA2 and SMA3 appear to be cold, dark, young mm cores, without evidence for current star formation. On the basis of the lack of line and mid-IR emission towards SMA2 and SMA3, we adopt a lower temperature limit of 20 K and an upper temperature limit of 40 K for these sources. The corresponding range of masses, column densities, and number densities for SMA2 and SMA3 are tabulated in Table 5. The mass of each (7-17 M_\odot for SMA2, 6-13 M_\odot for SMA3) is sufficient to form a low to intermediate mass star. No other cores are detected in the field to a 5σ upper limit of $M < 3M_\odot$ (at $T = 20$ K).

4.2. Velocity Structure and Outflows

Figure 10 shows a close-up view of the *Spitzer* 3-color IRAC image shown in Figure 1. The brightest mid-IR emission is extended along a NE-SW axis, approximately parallel to the axis of the UCH II region, but with an offset to the northwest of $\sim 2''$. The overall morphology of S255N is consistent with the multi-band bright mid-IR emission tracing the surface of the UCH II region, which is less dense to the southwest (of SMA1), as indicated by the diffuse “tail” of the cometary UC H II region extending in this direction. However, the detailed interpretation of the mid-IR emission toward S255N is complicated by the offset described above, and the sharp cutoff of the 3.6 and 8.0 μm emission along the southeast boundary of the UCH II region. Indeed, mid-IR emission is notably absent toward SMA2 and SMA3, as well as toward much of SMA1. A likely scenario for this behavior is absorption of the mid-IR emission by the high column density mm cores; in this scenario the bulk of the relatively cold mm cores must be in front of the UCH II region.

With the exception of SMA1, the molecular emission in S255N is not obviously associated with any continuum emission, and is therefore unlikely to be centrally heated. However, as described in §4.1 the H_2CO line ratios suggest the gas is warm. Thus, it is likely that

much of this emission is associated with outflow material, although the number of outflows and their driving source(s) are unclear. Published data on large-scale outflows in the region (e.g. Miralles et al. 1997; Richardson et al. 1985; Heyer et al. 1989; Ruiz et al. 1992) are unfortunately too low in angular resolution to be useful in distinguishing outflows associated with S255N from those associated with S255IR to the south, and/or the maps are swamped by emission from a large outflow flowing north from S255IR. Excluding the “SW” position, the relatively narrow linewidths of these S255N line emission regions suggest that they are density enhancements within a larger extended flow resolved out by the interferometer. The relative similarity of the line center velocities further suggests that the outflows are mostly in the plane of the sky.

The linear morphology of the (green) $4.5\ \mu\text{m}$ emission northeast of SMA1 is suggestive of an outflow (Fig. 10). Such $4.5\ \mu\text{m}$ nebulosity is a conspicuous feature of IRAC images of star forming regions. Recent analysis of the massive DR21 outflow, the best-studied example, has shown that H_2 line emission accounts for $\sim 50\%$ of the observed $4.5\ \mu\text{m}$ IRAC flux, and that the outflow morphology is almost identical in IRAC $4.5\ \mu\text{m}$ and narrow-band $2.122\ \mu\text{m}$ (H_2 1-0 S(1) line) images (Davis et al. 2007; Smith et al. 2006). In S255N, the $2.122\ \mu\text{m}$ H_2 clump S255:H2-3 lies at the base of the $4.5\ \mu\text{m}$ nebulosity; the H_2 clump is also coincident, within reported astrometric uncertainties, with our newly-reported water maser. Both the $2.122\ \mu\text{m}$ H_2 1-0 S(1) line and the $4.6947\ \mu\text{m}$ H_2 0-0 S(9) line, identified by Smith et al. (2006) as the dominant contributor to IRAC band 2, trace moderate-velocity shocks (Draine, Roberge, & Dalgarno 1983). Recent models by Smith & Rosen (2005) of shocks in dense protostellar molecular jets predict that the integrated H_2 line contribution to IRAC band 2 will be 5-14 times greater than to IRAC band 1 ($3.6\ \mu\text{m}$), consistent with the ratio of the emission seen in these bands toward the linear $4.5\ \mu\text{m}$ feature. The 44 GHz Class I methanol masers, five of which lie along the $4.5\ \mu\text{m}$ emission feature, provide further evidence for its identification as an outflow. Kurtz, Hofner, & Álvarez (2004) found that masers of this type are often found in association with such outflow tracers as SiO (IRAS 20126+4104, G31.41+0.31 and G34.26+0.15) and H_2 (IRAS 20126+4104). In G31.41+0.31, the 44 GHz methanol masers are also associated with thermal methanol emission (Kurtz, Hofner, & Álvarez 2004), which Liechti & Walmsley (1997) found traced shock/clump interfaces in the DR21 outflow. The parallels between these examples and S255N strongly suggest that the 44 GHz methanol masers, H_2CO , CH_3OH , SiO, H_2 , and $4.5\ \mu\text{m}$ emission extending northeast from SMA1-NE trace a molecular outflow from a protostar, probably SMA1-NE.

At the SW position, the broad lines with strong blue wings combined with the morphology of the H_2CO and CH_3OH channel maps are consistent with a blueshifted outflow lobe driven by SMA1-SW. Notably, no 44 GHz methanol masers coincide with the very strong

thermal CH_3OH emission of the SW line peak, although elsewhere in S255N the methanol maser flux densities are loosely correlated with the strength of thermal CH_3OH emission. The absence of masers towards the SW position suggests that the physical conditions are not appropriate for the collisional pumping of Class I methanol masers (Cragg et al. 1992; Plambeck & Menten 1990).

4.3. The Nature of SMA1

The complex kinematic behavior of the molecular line emission in the vicinity of SMA1 including SMA1-NE, SMA1-SW, and position “SW” (§3.3) is difficult to explain in the context of a single protostar. Though SMA1-NE and SMA1-SW could be interpreted as the blue and red-shifted lobes, respectively, of an outflow, this scenario does not explain the very blue-shifted emission further to the southwest at position “SW”. Rotation also seems like an unlikely explanation for the velocity gradient between SMA1-NE and SMA1-SW since the gradient is parallel to the direction of the two probable outflow regions: the $4.5\ \mu\text{m}$ emission to the northeast and “SW” to the southwest. Instead, the combination of the chemical and kinematic differentiation between SMA1-SW and SMA1-NE suggests the presence of two individual sources, one at $+7\ \text{km s}^{-1}$ and one at $+11.5\ \text{km s}^{-1}$. To investigate this possibility, in Figure 11 we show a uniform weighted SMA millimeter continuum image restored with a beam of $1''.0$ (~ 3 times smaller than the longest observed baseline), which essentially reveals the location of the clean components. The localization of clean components into two main regions in the vicinity of SMA1 suggests the presence of at least two sources separated by $\sim 1''.84$ (4800 AU). If these two clean component peaks correspond to real dust sources, their positions are in good agreement with the two kinematically distinct formaldehyde peaks ($< 0''.1$ and $< 0''.5$). The northeast component of the pair is also within $0''.2$ of the water maser. That two distinct protostars would exist with this separation is reasonable, as multiplicity of protostars has been observed on scales of $< 6,000$ AU (e.g. Megeath, Wilson, & Corbin 2005). Although the presence of two protostars is a plausible interpretation, it clearly requires higher resolution continuum observations for confirmation.

In any case, the molecular line emission from SMA1-NE and SMA1-SW is reminiscent of hot molecular cores (HMCs), particularly the detection of DCN and HC_3N . These molecules—like CH_3OH and H_2CO , which also show strong emission towards SMA1-NE and SMA1-SW—are present in the gas phase in HMCs because they have been evaporated from grain mantles (e.g. Caselli 2005; Szczepanski et al. 2005). Complex organic molecules such as HCOOCH_3 , however, are believed to be “daughter” species, formed in the gas phase by reactions of “parent” species such as H_2CO and CH_3OH (Caselli 2005). Thus, while SMA1-NE and

SMA1-SW do not exhibit the truly copious molecular emission observed towards some HMCs (e.g. Hatchell, Millar, & Rodgers 1998; Schilke et al. 2006), this is consistent with SMA1-NE and SMA1-SW being very young sources, in which gas-phase hot-core chemistry has not yet produced abundant complex organic molecules.

The line emission from the SMA1 sources is unusual in that the DCN(3-2) emission is stronger than HC₃N(24-23). By modeling deuterium chemistry, Roberts & Millar (2000) find that the steady-state abundance of DCN in molecular clouds is a complicated function of temperature and density (see their Figure 7), but generally higher at low metallicity. We note this because S255N is located approximately ($l \sim 192^\circ$) in the direction of the Galactic anticenter, and may have lower metallicity than inner-galaxy star-forming regions (Daflon & Cunha 2004; Afflerbach et al. 1997). Our SMA data, however, do not allow us to disentangle the effects of abundance and excitation on the strengths of DCN and HC₃N emission.

The geometry of a HMC located a few arcseconds ahead of the vertex of a cometary UCH II region has been seen in other objects observed at high angular resolution, and this notable configuration has led to much discussion on the energy source responsible for these HMCs. The best-studied case for external heating is G34.26+0.15, in which Watt & Mundy (1999) and Mookerjee et al. (2007) argue that HMC emission (characterized by complex nitrogen and oxygen-rich molecules) arises in gas heated by component C, the most evolved of three nearby UCH II regions. In the absence of extinction, a $1.1 \times 10^4 L_\odot$ source at the location of the 3.6 cm point source could heat SMA1-NE to ~ 37 K, and SMA1-SW to ~ 51 K, consistent only with the lower end of the range of plausible gas temperatures. In contrast, G29.96-0.02 is the prototype for a HMC located ahead of a cometary UCH II region and internally heated by a high mass protostellar object (De Buizer, Osorio, & Calvet 2005; Gibb, Wyrowski, & Mundy 2003). In G29.96-0.02, HMC emission is coincident with a resolved 1.4 mm continuum source, water maser spots, and a mid-IR sub-arcsecond point source (De Buizer, Osorio, & Calvet 2005; Gibb, Wyrowski, & Mundy 2003; Olmi et al. 2003, and references therein). In S255N, the arrangement of the 1.3 mm and 3.6 cm sources along with the presence of water maser emission coincident with the molecular emission closely resembles the case of G29.96-0.02. We favor the interpretation that one or more sources younger than the excitation source of the UCH II region are present and responsible for the compact dust and molecular line emission from SMA1, consistent with the interpretation of the hot core emission outlined above.

5. Conclusions

Our multiwavelength observations of S255N reveal significant new details in this luminous star-forming region. While the previously-identified UCH II region dominates the cm continuum and mid-IR emission, the 1.3 mm continuum emission has been resolved into three compact cores (SMA1, SMA2, and SMA3) clustered on scales of 0.1-0.2 pc. Dominated by dust emission, these cores range in mass from 6 to 35 M_{\odot} . There are no mid-infrared point source counterparts to any of the dust cores, suggesting an early evolutionary phase. The spectral line emission at the position of the brightest core, SMA1, is spatially compact and includes HC_3N , CN , DCN , CH_3OH , SiO , and H_2CO . SMA1 appears to be a developing hot core offset by a few thousand AU from the UCH II region. The chemical and kinematic structure toward SMA1 is suggestive of further multiplicity at these scales. A $4.5 \mu\text{m}$ linear feature emanating to the northeast of SMA1 is aligned with a cluster of methanol masers and likely traces a outflow from a protostar within SMA1. We conclude that S255N is actively forming a cluster of intermediate to high-mass stars. In addition, we speculate that some of the missing flux in the SMA continuum image could be in the form of additional compact low-mass, cold dust cores that lie below the sensitivity limit of our observations ($M \sim 3M_{\odot}$ at $T = 20 \text{ K}$). Higher-resolution and more sensitive observations are needed to search for additional protostars in S255N and other young protoclusters. Resolving individual protostars in regions like these is a necessary task to determine how dense these young protoclusters are, and how interactions among protostars in protoclusters may affect the process of star formation.

This work is based in part on observations made with the *Spitzer Space Telescope*, which is operated by the Jet Propulsion Laboratory, California Institute of Technology under a contract with NASA. This research has made use of NASA’s Astrophysics Data System Bibliographic Services and the SIMBAD database operated at CDS, Strasbourg, France. Research at the CSO is funded by the NSF under contract AST96-15025. CJC is supported by a National Science Foundation Graduate Research Fellowship and acknowledges partial support from a Wisconsin Space Grant Graduate Fellowship. CJC would like to thank the SMA and NRAO for student research support.

REFERENCES

Afflerbach, A., Churchwell, E., & Werner, M. W. 1997, *ApJ*, 478, 190

- Beltrán, M. T., Brand, J., Cesaroni, R., Fontani, F., Pezzuto, S., Testi, L., & Molinari, S. 2006, *A&A*, 447, 221
- Brand, J., & Blitz, L. 1993, *A&A*, 275, 67
- Caselli, P. 2005, *Cores to Clusters: Star Formation with Next Generation Telescopes*, 47
- Ceccarelli, C., Hollenbach, D.J., & Tielens, A.G.G.M. 1996, *ApJ*, 471, 400
- Cragg, D.M., Johns, K.P., Godfrey, P.D., Brown, R.D. 1992, *MNRAS*, 259, 203
- Crowther, P. A., & Conti, P. S. 2003, *MNRAS*, 343, 143
- Daflon, S., & Cunha, K. 2004, *ApJ*, 617, 1115
- Davis, C.J., Kumar, M.S.N., Sandell, G., Froebrich, D., Smith, M.D., & Currie, M.J. 2007, *MNRAS*, 374, 29
- De Buizer, J.M., Osorio, M., Calvet, N. 2005, *ApJ*, 635, 452
- Draine, B.T., Roberge, W.G., & Dalgarno, A. 1983, *ApJ*, 264, 485
- Emerson, D.T., Klein, U. & Haslam, C.G.T. 1979, *A&A*, 76, 92
- Fazio et al. 2004, *ApJS*, 154, 10
- Georgelin, Y.M., Georgelin, Y.P., & Roux, S. 1973, *A&A*, 25, 337
- Gibb, A.G., Wyrowski, F., & Mundy, L.G. 2003, in *SFChem 2002: Chemistry as a Diagnostic of Star Formation*, ed. C.L. Curry & M. Fich (Ottawa: NRC Press), 214
- Gutermuth, R. A., Megeath, S. T., Pipher, J. L., Williams, J. P., Allen, L. E., Myers, P. C., & Raines, S. N. 2005, *ApJ*, 632, 397
- Hatchell, J., Millar, T.J., & Rodgers, S.D. 1998, *A&A*, 332, 695
- Heyer, M. H., Snell, R. L., Morgan, J., & Schloerb, F. P. 1989, *ApJ*, 346, 220
- Howard, E.M., Pipher, J.L. & Forrest, W.J. 1997, *ApJ*, 481, 327
- Hunter, T.R., Benford, D.J. & Serabyn, E. 1996, *PASP*, 108, 1042
- Hunter, D.A. & Massey, P. 1990, *AJ*, 99, 846
- Itoh, Y., Tamura, M., Suto, H., Hayashi, S.S., Murakawa, K., Oasa, Y., Nakajima, Y., Kaifu, N., Kosugi, G., Usuda, T., & Doi, Y. 2001, *PASJ*, 53, 495

- Jaffe, D. T., Davidson, J. A., Dragovan, M., & Hildebrand, R. H. 1984, *ApJ*, 284, 637
- Kaufman, M.J., Hollenbach, D.J., & Tielens, A.G.G.M. 1998, *ApJ*, 497, 276
- Kurtz, S., Hofner, P., & Álvarez, C. V. 2004, *ApJS*, 155, 149
- Kurtz, S., Churchwell, E., & Wood, D. O. S. 1994, *ApJS*, 91, 659
- Lada, C. J., & Lada, E. A. 2003, *ARA&A*, 41, 57
- Liechti, S. & Walmsley, C.M. 1997, *A&A*, 321, 625
- Malafeev, S. Y., Zinchenko, I. I., Pirogov, L. E., & Johansson, L. E. B. 2005, *Astronomy Letters*, 31, 239
- Mangum, J. G., Plambeck, R. L., & Wootten, A. 1991, *ApJ*, 369, 169
- Mangum, J.G., & Wootten, A. 1993, *ApJS*, 89, 123
- Megeath, S. T., Wilson, T. L., & Corbin, M. R. 2005, *ApJ*, 622, L141
- Mezger, P. G., Chini, R., Kreysa, E., Wink, J. E., & Salter, C. J. 1988, *A&A*, 191, 44
- Minier, V., Burton, M. G., Hill, T., Pestalozzi, M. R., Purcell, C. R., Garay, G., Walsh, A. J., & Longmore, S. 2005, *A&A*, 429, 945
- Miralles, M. P., Salas, L., Cruz-Gonzalez, I., & Kurtz, S. 1997, *ApJ*, 488, 749
- Moffat, A. F. J., Jackson, P. D., & Fitzgerald, M. P. 1979, *A&AS*, 38, 197
- Mookerjee, B., Casper, B., Mundy, L.G., & Looney, L.W. 2007, *astroph/#0701827*
- Muench, A. A., Lada, E. A., Lada, C. J., & Alves, J. 2002, *ApJ*, 573, 366
- Olmi, L., Cesaroni, R., Hofner, P., Kurtz, S., Churchwell, E., & Walmsley, C.M. 2003, *A&A*, 407, 225
- Ossenkopf, V., & Henning, Th. 1994, *A&A*, 291, 943
- Plambeck, R. L., & Menten, K. M. 1990, *ApJ*, 364, 555
- Rengarajan, T. N., & Ho, P. T. P. 1996, *ApJ*, 465, 363
- Richardson, K. J., White, G. J., Gee, G., Griffin, M. J., Cunningham, C. T., Ade, P. A. R., & Avery, L. W. 1985, *MNRAS*, 216, 713

- Roberts, H., & Millar, T.J. 2000, *A&A*, 361, 388
- Ruiz, A., Rodriguez, L. F., Canto, J., & Mirabel, I. F. 1992, *ApJ*, 398, 139
- Schilke, P., Comito, C., Thorwirth, S., Wyrowski, F., Menten, K. M., Güsten, R., Bergman, P., & Nyman, L.-Å. 2006, *A&A*, 454, L41
- Smith, H.A., Hora, J.L., Marengo, M., & Pipher, J.L. 2006, *ApJ*, 645, 1264
- Smith, M.D., & Rosen, A. 2005, *MNRAS*, 357, 1370
- Snell, R. L., & Bally, J. 1986, *ApJ*, 303, 683
- Sutton, E.C., Blake, G.A., Masson, C.R., & Phillips, T.G. 1985, *ApJS*, 58, 341
- Szczepanski, J., Wang, H., Doughty, B., Cole, J., & Vala, M. 2005, *ApJ*, 626, L69
- Wang, N., Hunter, T.R., Benford, D.J., Serabyn, E., Lis, D.C., et al. 1996, *Applied Optics*, 35, 6629
- Watt, S., & Mundy, L. G. 1999, *ApJS*, 125, 143
- Zinchenko, I., Henning, T., & Schreyer, K. 1997, *A&AS*, 124, 385

Table 1. Properties of millimeter continuum sources in S255N

Source	J2000 coordinates		$I_{1.3\text{mm}}$	Size ^a	$F_{1.3\text{mm}}$ ^b	T_{b} ^c
	α (h m s)	δ ($^{\circ}$ ' ")	(Jy/b)	[" \times " ($^{\circ}$)]	(Jy)	(K)
SMA1	06 12 53.67	+18 00 26.9	0.29	3.9 \times 2.0 (17.4)	0.58 ± 0.12	1.84
SMA2	06 12 52.97	+18 00 31.9	0.09	2.2 \times 1.6 (97.5)	0.12 ± 0.02	0.82
SMA3	06 12 53.69	+18 00 18.5	0.05	5.2 \times <1.3 (169.6)	0.09 ± 0.02	0.33
Total					0.79 ± 0.16	

^aDeconvolved source size determined by fitting a single Gaussian component to each source. The SMA beam is $4''.7 \times 2''.4$ (P.A.= -45.65°).

^bUncertainties include 20% calibration uncertainty.

^cBrightness temperature computed using the Rayleigh-Jeans approximation.

Table 2. Molecular species and transitions observed in S255N

Species	Transition	Frequency (GHz)	E_{upper}/k (K)
SiO	5 \rightarrow 4	217.104980	31.2
DCN	3 \rightarrow 2	217.238538	20.9
H ₂ CO	3 _{0,3} \rightarrow 2 _{0,2}	218.222192	21.0
HC ₃ N	24 \rightarrow 23	218.324723	131
CH ₃ OH	4 _{+2,2,0} \rightarrow 3 _{+1,2,0}	218.440050	45.5
H ₂ CO	3 _{2,2} \rightarrow 2 _{2,1}	218.475632	68.1
H ₂ CO	3 _{2,1} \rightarrow 2 _{2,0}	218.760066	68.1
CN ^{a,b}	2 _{0,3,3} \rightarrow 1 _{0,2,2}	226.874191	16.4
CN ^{a,c}	2 _{0,3,4} \rightarrow 1 _{0,2,3}	226.874781	16.4
CN ^a	2 _{0,3,2} \rightarrow 1 _{0,2,1}	226.875896	16.4
CN	2 _{0,3,2} \rightarrow 1 _{0,2,2}	226.887420	16.4
CN	2 _{0,3,3} \rightarrow 1 _{0,2,3}	226.892128	16.4
HC ₃ N	25 \rightarrow 24	227.418905	142

^aThese components are blended in our spectra.

^bThe CN hyperfine components at frequencies lower than this one lie outside of our observed band-pass.

^cThis transition is used to set the velocity scale for CN in Fig 8.

Table 3. Spectral line positions

Name	J2000 coordinates	
	α (^h ^m ^s)	δ ([°] ['] ^{''})
SMA1-NE	06 12 53.73	+18 00 27.8
SMA1-SW	06 12 53.64	+18 00 25.4
SW	06 12 53.45	+18 00 23.0
NE	06 12 53.76	+18 00 33.2
N	06 12 53.70	+18 00 39.8
NW	06 12 52.86	+18 00 36.2

Table 4. Fitted line properties

Position	$\text{H}_2\text{CO}(3_{0,3}-2_{0,2})$			CH_3OH			DCN			$\text{HC}_3\text{N}(24-23)$		
	Center km s^{-1}	Width km s^{-1}	$\int S_\nu dv$ $\text{Jy b}^{-1} * \text{km s}^{-1}$	Center km s^{-1}	Width km s^{-1}	$\int S_\nu dv$ $\text{Jy b}^{-1} * \text{km s}^{-1}$	Center km s^{-1}	Width km s^{-1}	$\int S_\nu dv$ $\text{Jy b}^{-1} * \text{km s}^{-1}$	Center km s^{-1}	Width km s^{-1}	$\int S_\nu dv$ $\text{Jy b}^{-1} * \text{km s}^{-1}$
SMA1-NE	6.9(0.3) ^a	5.9(0.6) ^a	5.5(0.7) ^a	6.6(0.3) ^c	3.4(0.9) ^c	0.9(0.3) ^c	8.2(0.1)	3.3(0.2)	5.2(0.4)	6.3(0.3) ^a	3.5(0.8) ^a	1.9(0.6) ^a
SMA1-SW	12.1(0.1)	2.9(0.2)	4.2(0.3)	11.2(0.1)	2.4(0.2)	3.1(0.4)	10.7(0.3) ^b	5.6(0.7) ^b	3.1(0.5) ^b	9.5(0.8) ^a	11.2(2.1) ^a	3.0(0.7) ^a
SW	6.3(0.1)	9.2(0.4)	24.3(1.2)	7.8(0.1)	6.9(0.3)	13.4(0.8)
NE	8.3(0.1)	2.9(0.3)	2.4(0.4)	8.3(0.2)	2.5(0.4)	1.6(0.4)
N	11.5(0.1)	2.6(0.3)	2.4(0.3)	10.1(0.2)	2.5(0.5)	1.5(0.4)
NW	8.9(0.2)	5.8(0.6)	5.3(0.7)	8.3(0.2) ^a	5.7(0.5) ^a	3.7(0.5) ^a

^aNot well fit by a single Gaussian.

^bGaussian fit encompasses two blended components.

^cParameters for second-strongest velocity component. Strongest component is very similar to that towards SMA1-SW.

Table 5. Range of estimated masses of dust cores in S255N

Source ^a	κ (cm ² g ⁻¹)	T_{dust} (K)	τ_{dust} (1.3mm)	M (M_{\odot})	N_{H_2} ^b (10 ²³ cm ⁻²)	n_{H_2} ^b (10 ⁶ cm ⁻³)
SMA1 ^c	1	40-100	0.04-0.02	35-13	10.5-3.8	15.9-5.8
SMA2	1	20-40	0.02-0.01	17-7	5.0-2.2	7.6-3.3
SMA3	1	20-40	0.01-0.01	13-6	3.9-1.7	5.9-2.5
Total				65-26		

^aAssumed distance is 2.6 kpc.

^bBeam-averaged quantities. The SMA beam is $4''.7 \times 2''.4$ (P.A. = -45.65°).

^cThe mass of SMA1 was calculated using the 1.3 mm flux density less the estimated free-free contribution of 20 mJy.

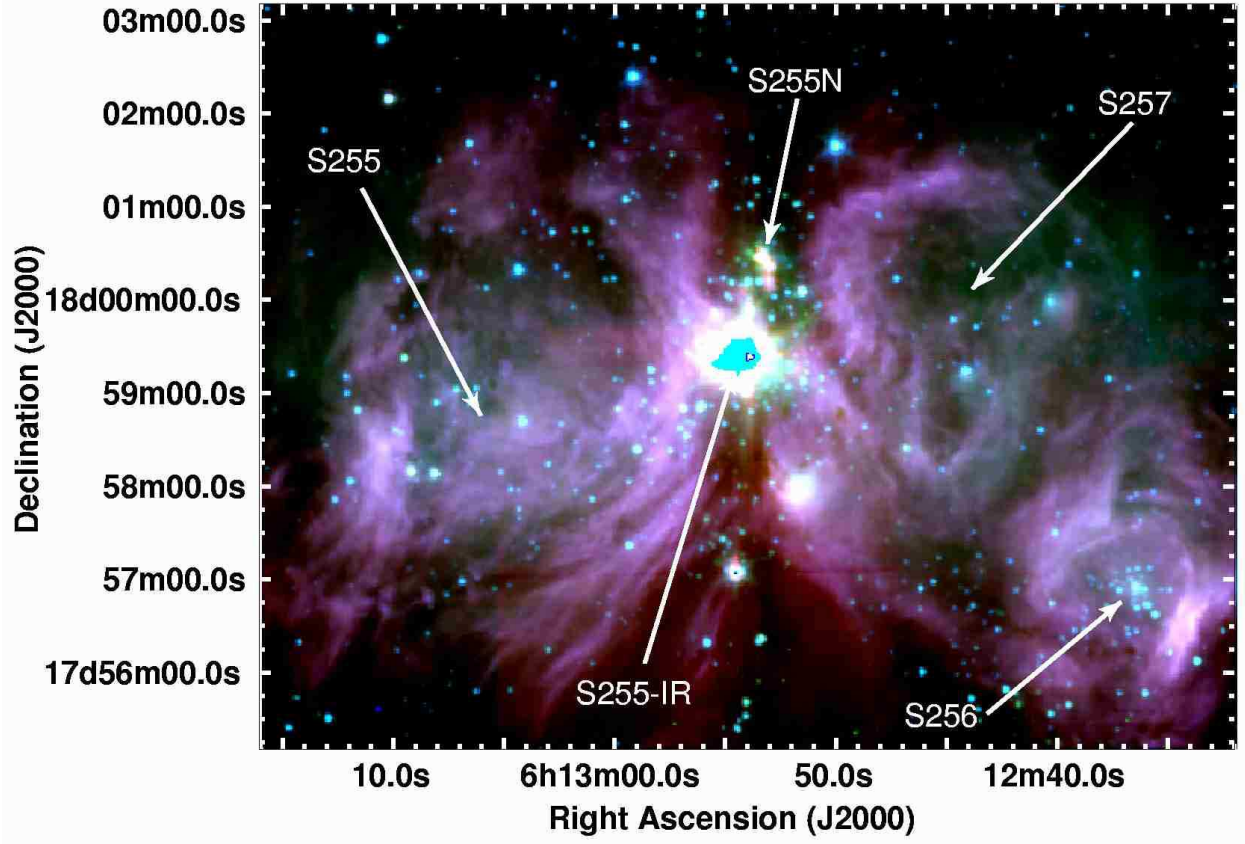


Fig. 1.— Three-color *Spitzer* IRAC image of S255N and its surroundings showing $8.0\ \mu\text{m}$ (red), $4.5\ \mu\text{m}$ (green), and $3.6\ \mu\text{m}$ (blue). S255N lies in a complex region of past and ongoing massive star-formation.

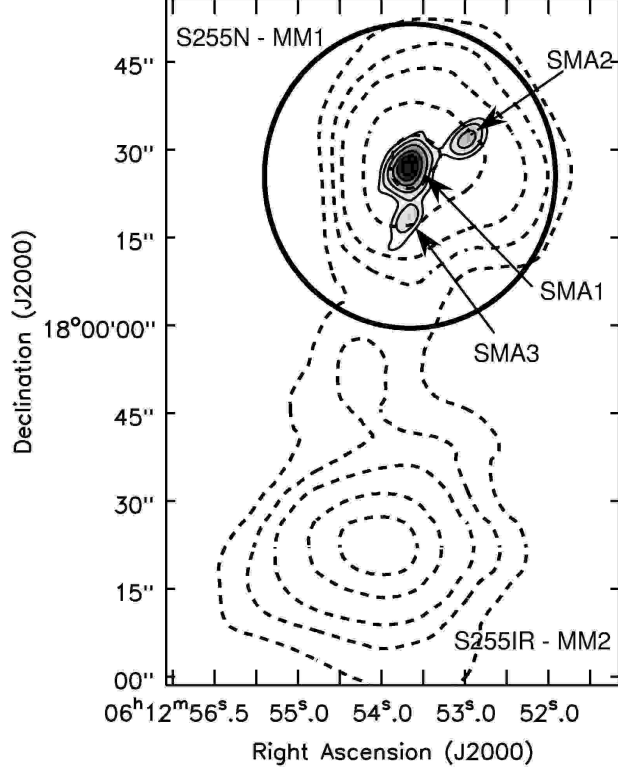


Fig. 2.— Greyscale and solid contours of the SMA 1.3 mm continuum with dotted contours of the CSO 350 μm continuum superposed. The primary beam of the SMA (56'' at 218.7 GHz) is indicated with a black circle. Naming conventions for mm and submm sources used in the literature and in this paper are also indicated. The black 1.3 mm contour levels are $(-3, 3, 7, 15, 31, 47, 63) \times 4 \text{ mJy beam}^{-1}$ (the rms noise), observed with a $4''.7 \times 2''.4$ (P.A. = -45.65°) beam. The dotted 350 μm contour levels are $(2, 2.5, 3, 4, 5) \times 16.5 \text{ Jy beam}^{-1}$, resolution 15''.

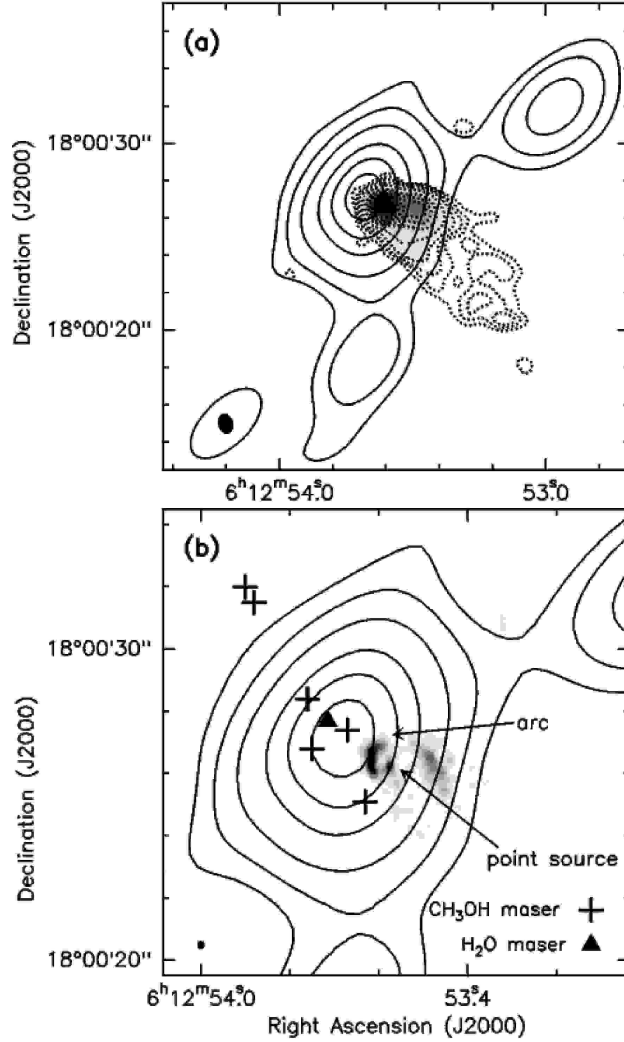


Fig. 3.— (a) Black contours of the SMA 1.3 mm continuum, observed with a $4''.7 \times 2''.4$ (P.A.= -45.65°) beam, with greyscale and dotted contours of the 3.6 cm continuum, observed with an $1''.03 \times 0''.84$ beam (P.A.= -81.42°), superposed. The black 1.3 mm contour levels are $(-3, 3, 7, 15, 31, 47, 63) \times 4 \text{ mJy beam}^{-1}$ (the rms noise). The dotted 3.6 cm contour levels are $(-3, 3, 5, 7, 11, 21, 41, 61, 81, 101, 121, 161) \times 34 \mu\text{Jy beam}^{-1}$ (the rms noise). The SMA beam (black ellipse) and VLA beam (filled black ellipse) are plotted at lower left. (b) Black contours of the SMA 1.3 mm continuum with greyscale of high-resolution ($0''.27 \times 0''.23$, P.A.= 77.51°) 3.6 cm continuum superposed. The positions of methanol masers and of the newly-reported water maser are marked. The VLA beam (filled black ellipse) is plotted at lower left.

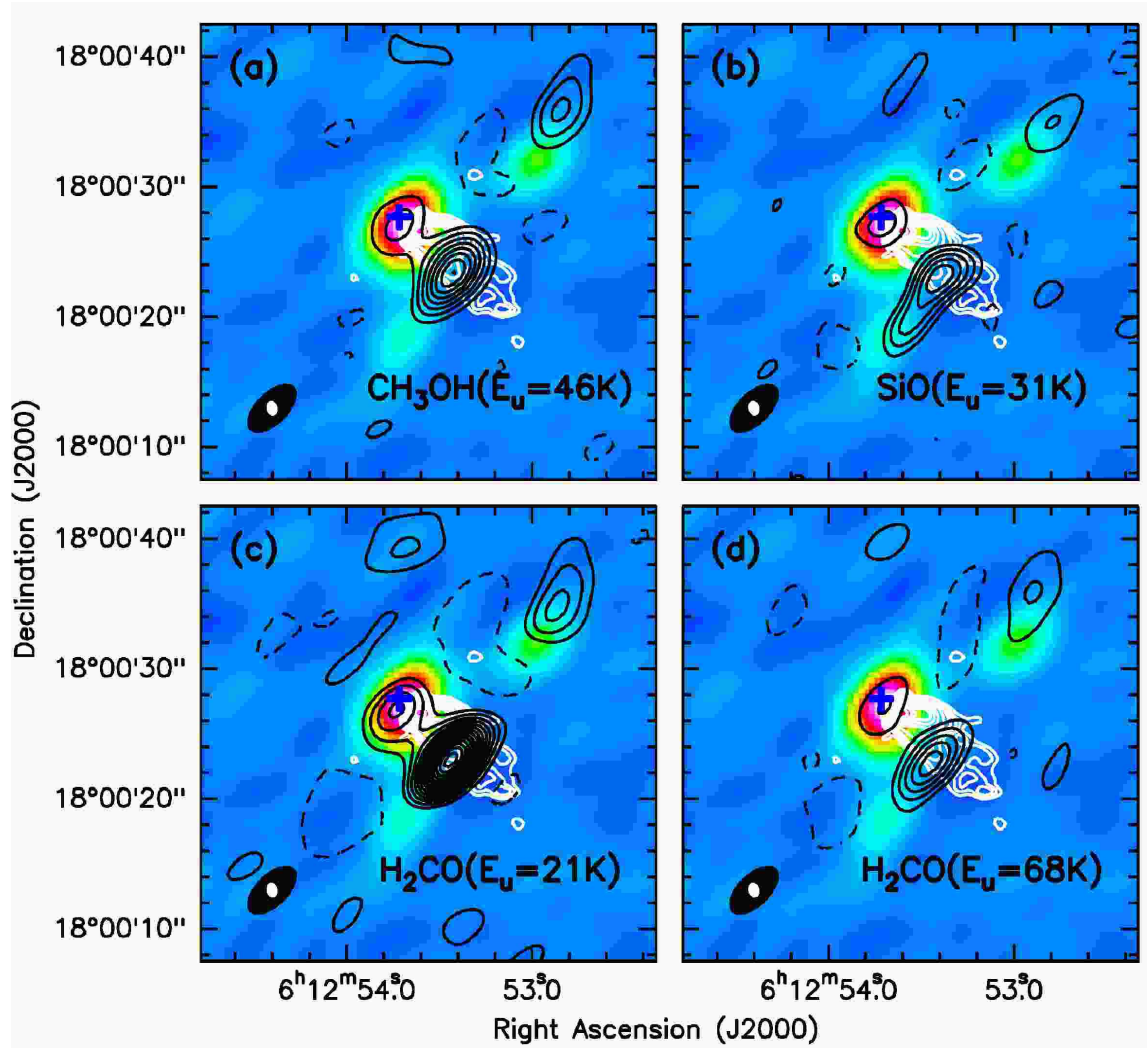


Fig. 4.— (a-d) Colorscale of the 1.3 mm continuum with black integrated intensity contours for molecules that exhibit emission from multiple positions. The molecular species and upper state energies are indicated in the lower right of each panel (also see Table 2). The white contours show 3.6 cm emission from the UC H II region G192.584-0.041. The blue cross marks the position of the newly detected water maser. The black integrated intensity contour levels are $(-3, 3, 5, 7, 9, 11, 13, 15, 17, 19, 21, 23, 25, 27, 29) \times$ the rms noise levels: (a) CH₃OH $0.82 \text{ Jy beam}^{-1} \text{ km s}^{-1}$, (b) SiO $1.35 \text{ Jy beam}^{-1} \text{ km s}^{-1}$, (c) H₂CO $3_{0,3} \rightarrow 2_{0,2}$ $0.8 \text{ Jy beam}^{-1} \text{ km s}^{-1}$, (d) H₂CO $3_{2,2} \rightarrow 2_{2,1}$ $0.76 \text{ Jy beam}^{-1} \text{ km s}^{-1}$. The white 3.6 cm contour levels are $(-3, 3, 5, 7, 11, 21, 41, 61, 81, 101, 121, 161) \times 34 \mu\text{Jy beam}^{-1}$ (the rms noise). The $4''.7 \times 2''.4$ (P.A. = -45.65°) SMA beam (filled black ellipse) and $1''.03 \times 0''.84$ (P.A. = -81.42°) VLA beam (filled white ellipse) are shown at lower left in each panel.

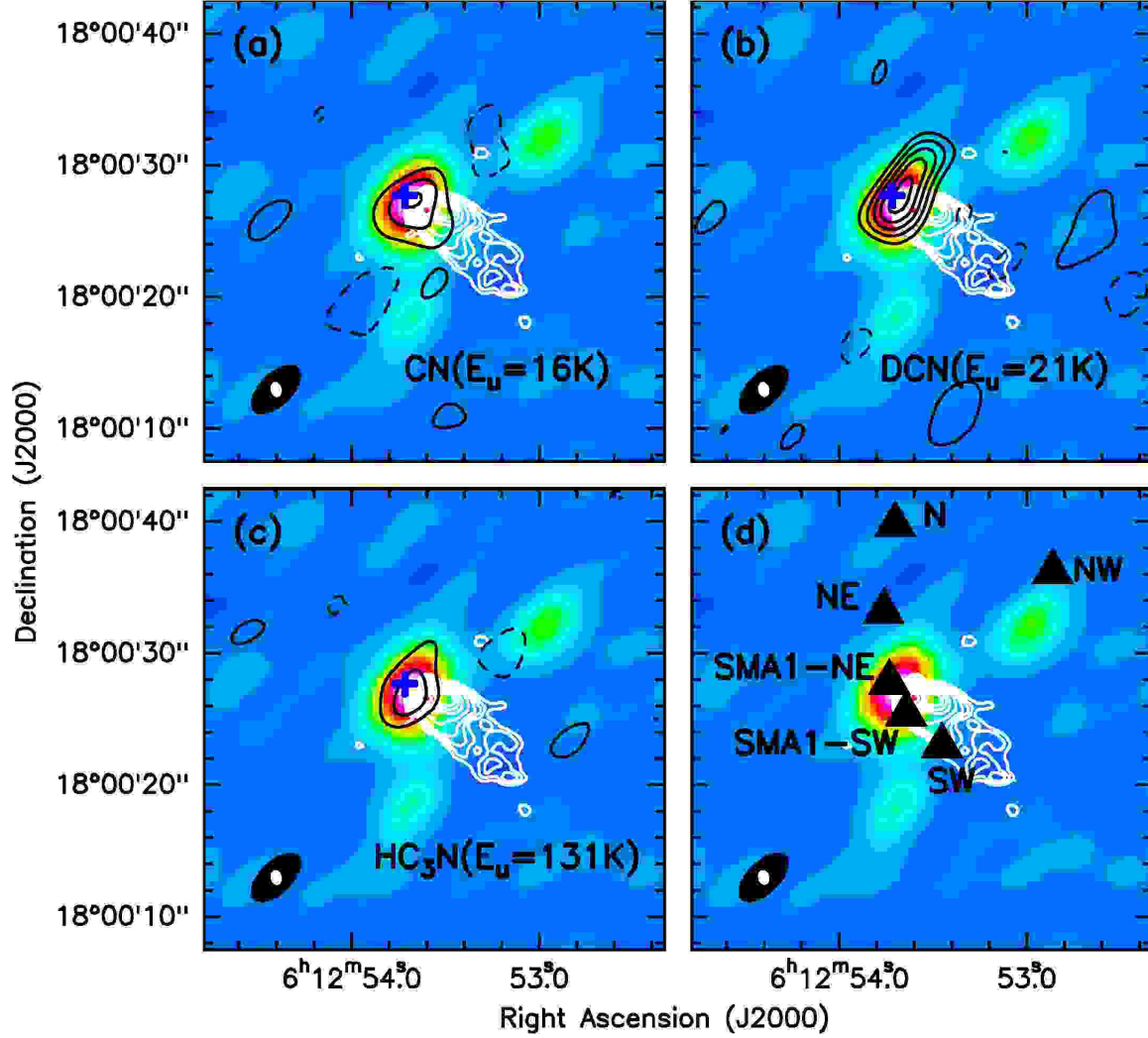


Fig. 5.— (a-c) Similar to Figure 4a-d except integrated intensity images are shown for molecules that are only detected in the vicinity of SMA1. The black integrated intensity contour levels are $(-3, 3, 5, 7, 9, 11) \times$ the rms noise levels: (a) CN $0.9 \text{ Jy beam}^{-1} \text{ km s}^{-1}$, (b) DCN $0.55 \text{ Jy beam}^{-1} \text{ km s}^{-1}$, and (c) HC_3N $24 \rightarrow 23$ $0.68 \text{ Jy beam}^{-1} \text{ km s}^{-1}$. (d) Finding chart for representative line profiles shown in Figures 7 & 8 and discussed in §3.3.

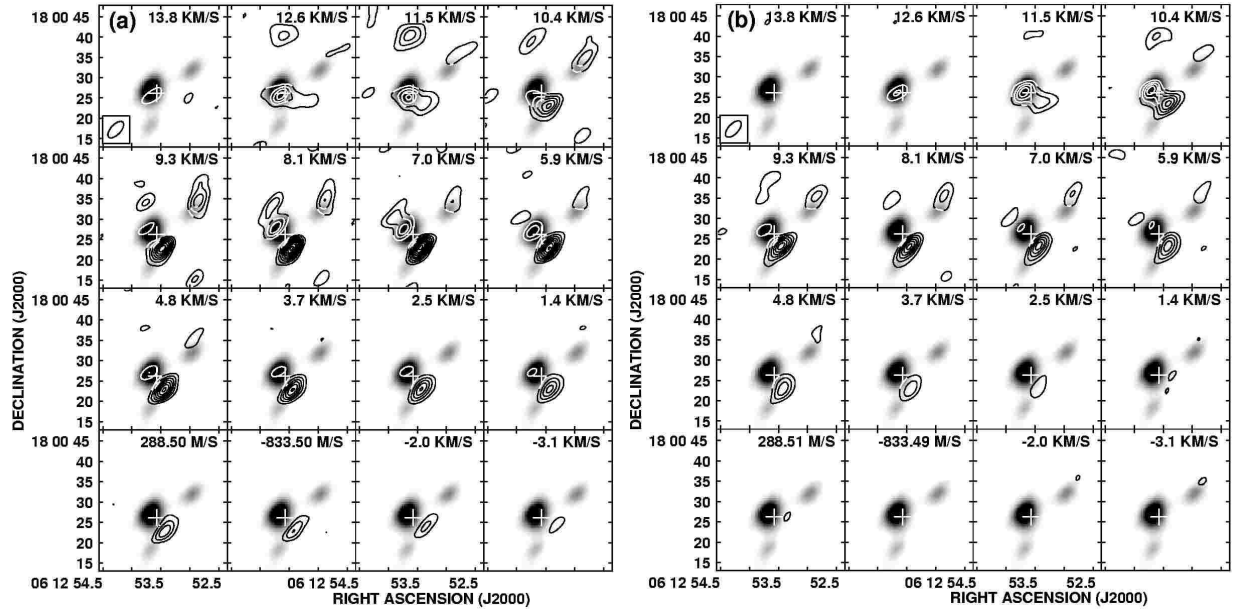


Fig. 6.— Channel maps of (a) $\text{H}_2\text{CO}(3_{0,3}-2_{0,2})$ and (b) CH_3OH , showing line emission (contours) overlaid on the 1.3 mm continuum (greyscale). The contours levels are (1, 2, 3, 4, 5, 6, 7, 8, 9) $\times 0.28 \text{ Jy beam}^{-1}$. Each panel is labeled with the channel velocity. The position of the 3.6 cm point source is marked with a white cross.

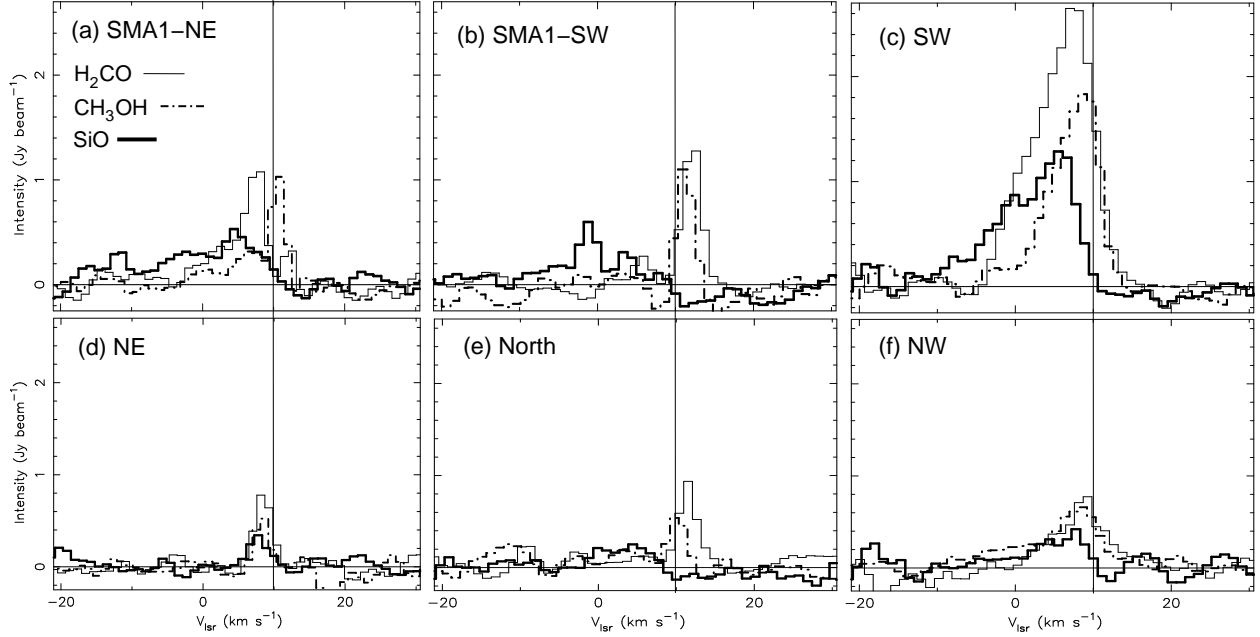


Fig. 7.— Representative line profiles for molecules that exhibit emission from multiple positions, demonstrating the wide range of velocity and chemical behavior observed. The positions for which spectra are presented are indicated on Figure 5d and listed in Table 3. A vertical line is drawn at 10 km s^{-1} for reference.

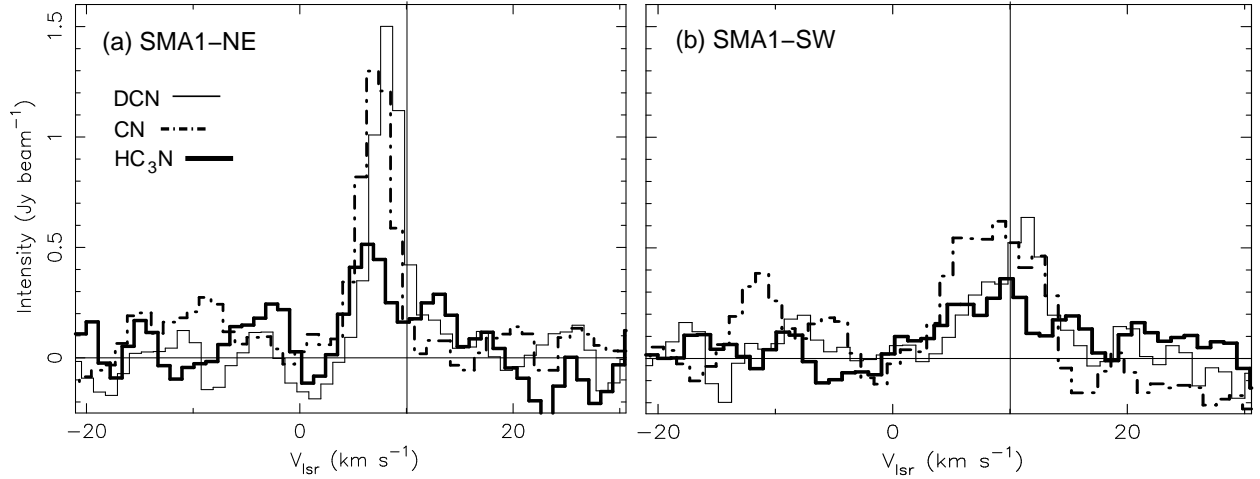


Fig. 8.— Representative line profiles for molecules that have their strongest emission towards SMA1. The positions for which spectra are presented are indicated on Figure 5d and listed in Table 3. A vertical line is drawn at 10 km s^{-1} for reference. Note that the vertical scale is not the same as in Figure 7. For CN, the weaker features offset by -16 and -22 km s^{-1} from the main feature are due to the hyperfine components (see Table 2).

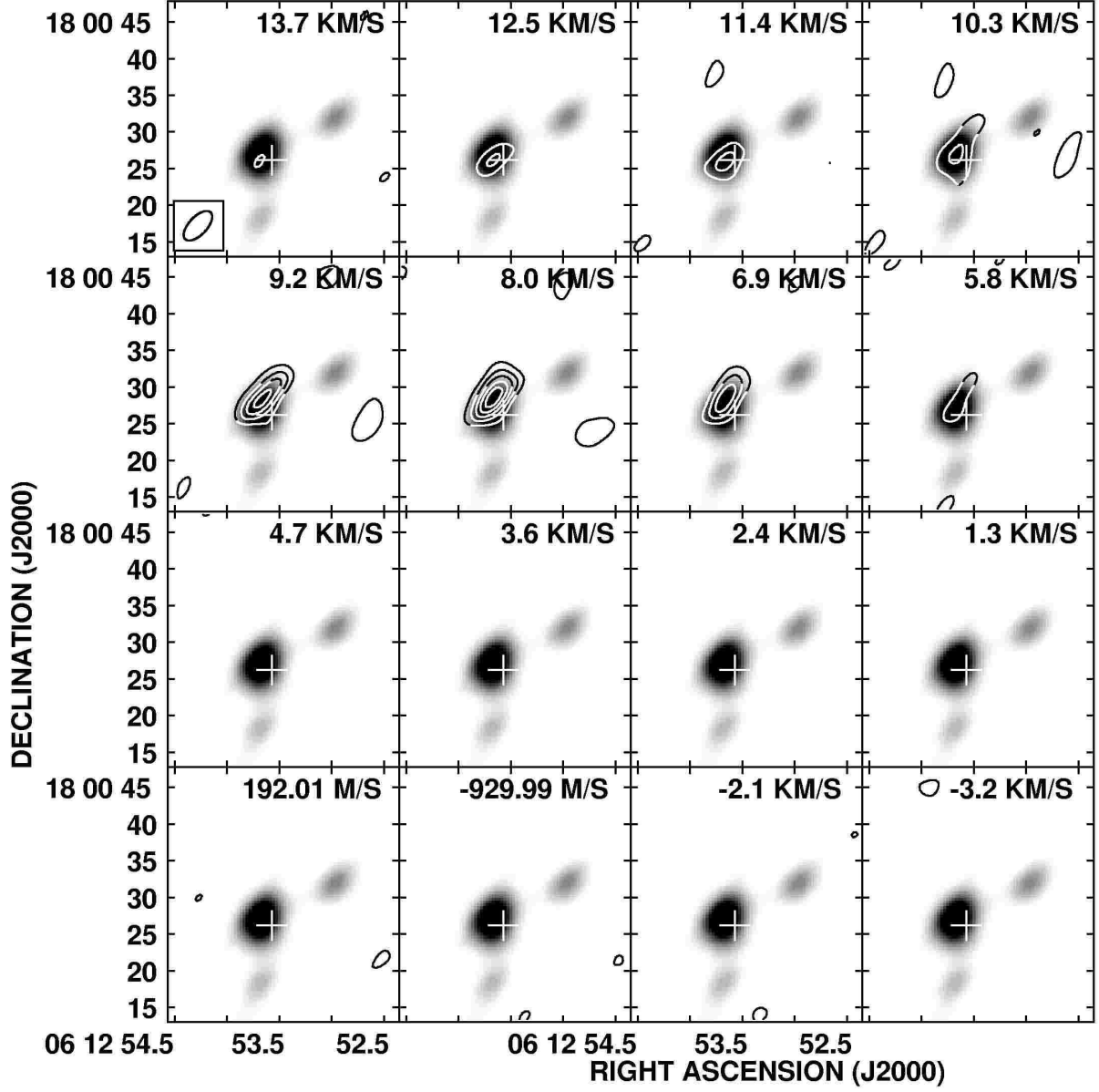


Fig. 9.— Channel maps of DCN emission (contours) overlaid on the 1.3 mm continuum (greyscale). Each panel is labeled with the channel velocity. The position of the 3.6 cm point source is marked with a white cross.

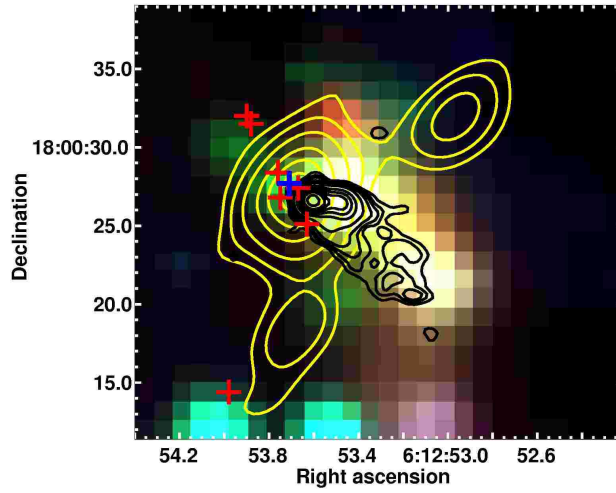


Fig. 10.— Close-up three-color *Spitzer* IRAC image of S255N showing mid-IR emission offset to the NW of the UC H II region with yellow SMA 1.3 mm and black 3.6 cm contours superposed. The colorscale correspond to: $8.0\ \mu\text{m}$ (red), $4.5\ \mu\text{m}$ (green), and $3.6\ \mu\text{m}$ (blue). The yellow SMA 1.3 mm continuum contour levels are $(3, 7, 15, 31, 47, 63) \times 4\ \text{mJy beam}^{-1}$ (the rms noise). The black VLA 3.6 cm continuum contour levels are $(3, 5, 7, 11, 21, 41, 61, 81, 101, 121, 161) \times 34\ \mu\text{Jy beam}^{-1}$ (the rms noise). Positions of Class I CH_3OH masers from Kurtz, Hofner, & Álvarez (2004) are marked with red crosses, and the position of the newly-reported water maser is marked with a blue cross.

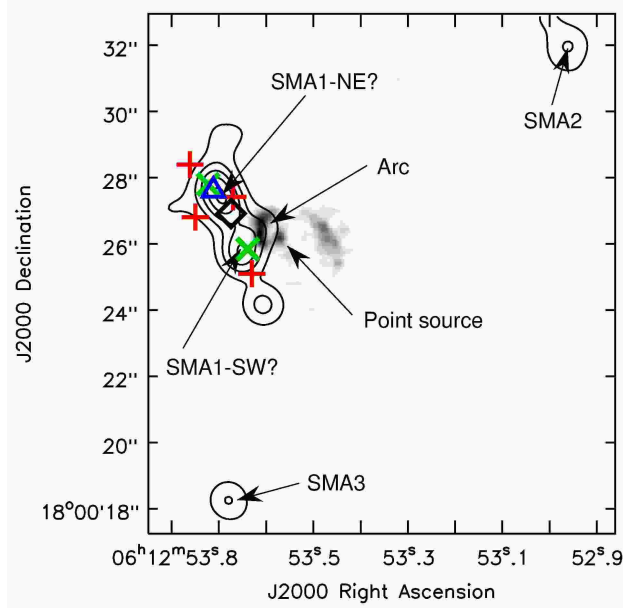


Fig. 11.— Greyscale image of the high resolution VLA 3.6 cm emission shown in Figure 3b with SMA 1.3 mm uniform weighted continuum contours superposed. The 1.3 mm image was restored with a $1''$ beam (~ 3 times smaller than the longest observed baseline) which essentially shows regions where clean components are concentrated. Red $+$ symbols show the 44 GHz methanol maser positions, the blue \triangle shows the H_2O maser position, the green \times symbols show the peak locations of the ~ 7 (SMA1-NE) and $\sim 11.5 \text{ km s}^{-1}$ (SMA1-SW) H_2CO components, and the black \diamond shows the location of SMA1 reported in Table 1. The localization of clean components into two distinct regions in the vicinity of SMA1 suggests the presence of at least two continuum sources; this result requires confirmation by higher resolution mm/submm data.